

# Structural and Statistical Audio Texture Knowledge Distillation (SSATKD) for Passive Sonar Classification

Jarin Ritu, Amirmohammad Mohammadi, Davelle Carreiro, Alexandra Van Dine, Joshua Peeples

**Abstract**—Knowledge distillation has been successfully applied to various audio tasks, but its potential in underwater passive sonar target classification remains relatively unexplored. Existing methods often focus on high-level contextual information while overlooking essential low-level audio texture features needed to capture local patterns in sonar data. To address this gap, the Structural and Statistical Audio Texture Knowledge Distillation (SSATKD) framework is proposed for passive sonar target classification. SSATKD combines high-level contextual information with low-level audio textures by utilizing an Edge Detection Module for structural texture extraction and a Statistical Knowledge Extractor Module to capture signal variability and distribution. Experimental results confirm that SSATKD improves classification accuracy while optimizing memory and computational resources, making it well-suited for resource-constrained environments.

**Impact Statement**—The SSATKD framework has the potential to significantly advance the field of passive sonar signal classification by enhancing performance while reducing computational overhead. This improvement is crucial for applications like autonomous underwater vehicle operations, and marine habitat monitoring, enabling more efficient real-time operations in environments which do not allow for extensive computational resources.

**Index Terms**—Knowledge distillation, Passive sonar, Audio Texture

## I. INTRODUCTION

Classifying signals in passive sonar systems is crucial for various applications, including marine biology, environmental monitoring, and underwater infrastructure management [1], [2]. Passive sonar uses sound waves to detect objects of

interest, such as vessels and marine life, without active emission of any signals [3]. Passive sonar signal classification presents unique challenges due to the inherent complexities of underwater environments [4]. Low signal-to-noise ratios (SNRs), high variability in acoustic signatures [5], [6], and signal distortion during propagation make it difficult to detect and classify sonar signals accurately [7]. Traditional signal processing techniques such as low frequency analysis and recording (LOFAR) spectra [8] and, detection of envelope modulation on noise (DEMON) [9] often struggle to deliver optimal results in such noisy and variable conditions [5]. To address these challenges, researchers have increasingly turned to advanced machine learning techniques, such as ensemble learning, where multiple models are trained on the same dataset, and their predictions are combined to improve accuracy [10]. While effective, ensemble models can be resource-intensive, especially with large neural networks [11]. This has led to growing interest in methods such as pruning weights from larger neural networks [12], quantizing networks to use fewer bits for weights and activations [13] and distilling knowledge from larger networks into smaller ones [10].

In a similar vein, knowledge distillation, first proposed by Hinton [10] and has become a popular approach for compressing deep networks without sacrificing performance [14]. The key idea is to use soft probabilities (or “logits”) generated by a larger “teacher network” to guide a smaller “student” network, alongside the standard class labels. These soft probabilities provide more information than the class labels alone, enabling the student network to learn more effectively. This process allows the student to replicate the teacher’s performance while using fewer resources, making the student network ideal for deployment on resource-constrained devices or in real-time applications [14], [15]. Despite success in other fields such as computer vision [16] and natural language processing [17], the application of knowledge distillation in underwater passive sonar target classification has been relatively underexplored.

While previous knowledge distillation methods effectively capture high-level contextual knowledge [18] or final response knowledge [19], finer texture details are often overlooked. Texture features can play an important role in passive sonar classification, as they help capture local patterns and variations. These subtle differences can be critical for distinguishing between different types of sonar signals. By incorporating texture information into the distillation process, the classification performance of sonar signals may be improved. A novel framework, Structural and Statistical Audio Texture

DISTRIBUTION STATEMENT A. Approved for public release. Distribution is unlimited. This material is based upon work supported by the Under Secretary of Defense for Research and Engineering under Air Force Contract No. FA8702-15-D-0001. Any opinions, findings, conclusions or recommendations expressed in this material are those of the author(s) and do not necessarily reflect the views of the Under Secretary of Defense for Research and Engineering. © 2024 Massachusetts Institute of Technology. Delivered to the U.S. Government with Unlimited Rights, as defined in DFARS Part 252.227-7013 or 7014 (Feb 2014). Notwithstanding any copyright notice, U.S. Government rights in this work are defined by DFARS 252.227-7013 or DFARS 252.227-7014 as detailed above. Use of this work other than as specifically authorized by the U.S. Government may violate any copyrights that exist in this work. [https://github.com/Advanced-Vision-and-Learning-Lab/SSTKAD\\_Lightning](https://github.com/Advanced-Vision-and-Learning-Lab/SSTKAD_Lightning)

Jarin Ritu, Amirmohammad Mohammadi, and Joshua Peeples are with the Department of Electrical and Computer Engineering, Texas A&M University, College Station, TX, USA (e-mail: jarin.ritu@tamu.edu; amir.m@tamu.edu; jpeeples@tamu.edu).

Davelle Carreiro and Alexandra Van Dine are with the Massachusetts Institute of Technology Lincoln Laboratory, Lexington, MA, USA (e-mail: davelle.carreiro@ll.mit.edu; alexandra.vandine@ll.mit.edu).

Knowledge Distillation (SSATKD), is proposed to efficiently transfer both low-level texture knowledge and high-level final responses from the teacher model to the student model. The SSATKD framework integrates two key modules for capturing structural and statistical texture information.

Overall, contributions of this work are as follows:

- In-depth analysis of different knowledge distillation strategies (*e.g.*, teacher-student architectures, loss functions)
- Incorporation of a novel Edge Detection Module for extracting structural texture
- Implementation of 2D Earth Mover's Distance (EMD) loss to quantify differences in statistical textures

## II. RELATED WORK

### A. Acoustic Texture Analysis for Sonar Signals

In audio data analysis, parallels can be drawn between sound and visual textures [20] which can be categorized into structural and statistical aspects [21]. In 1D audio waveforms, time represents the temporal dimension, and amplitude reflects the intensity of the sound at each time point [22]. Temporal dependency in audio signals mirrors the spatial dependency observed in 2D images, wherein neighboring pixels exhibit spatial relationships [22]. The repetitive patterns or rhythms in audio signals correspond to structural textures in images, revealing regularity and patterns in the sound. These structural textures capture the arrangement of elements within the signal, providing insights into recurring patterns present in the audio data. Meanwhile, amplitude variations in audio signals reflect statistical textures, similar to the intensity values observed in images [23]. These statistical textures encapsulate information about the distribution and variability of signal amplitudes, offering insight into the distribution and characteristics of the audio signal [22].

Recent efforts have explored audio classification algorithms by treating time-frequency representations of audio signals as images, a concept inspired by biologically motivated work on object recognition [24], [25]. By drawing parallels between the characteristics of images and 2D time-frequency representations, methods such as Gabor filters and wavelet transforms can extract meaningful texture information from the data [26], [27]. These textures are simpler and more consistent than complex sounds like speech or music, motivating the need for improved sound recognition and auditory representation in passive sonar systems [28].

### B. Deep Learning Methods for Passive Sonar Classification

Recent advancements in passive sonar classification have focused on deep learning methods that automatically extract features from time-frequency representations of sonar signals. Traditional techniques such as LOFAR, DEMON, and Mel-Frequency Cepstral Coefficients (MFCC) are commonly used to convert raw sonar data into Spectrograms or Cepstral features, which are then input into neural networks for classification [4], [26]. Deep neural networks (DNNs), particularly convolutional neural networks (CNNs), have proven more

effective in capturing both spatial and temporal features from these sonar spectrograms [29]. Recurrent neural networks (RNNs) and long short-term memory networks (LSTMs) have also been applied to model temporal dependencies, especially in ship-radiated noise, where sequential information plays a critical role [30], [31].

Hybrid architectures, such as the combination of CNNs and LSTMs, have further improved classification performance by capturing both spatial and temporal features [32], [33]. Additionally, multi-modal deep learning approaches that fuse features from different domains, such as audio and visual data, have shown promise for enhancing underwater target classification [34]. However, all of these methods can be computationally expensive and often require large datasets, limiting their application in real-time or resource-constrained environments.

### C. Knowledge Distillation Vs Transfer Learning

Transfer learning is a widely used strategy in machine learning, particularly when training data is limited or difficult to collect [35], [36]. Further, transfer learning has been widely used in audio tasks, such as sound event tagging [37], emotional audio research [38], [35], and environmental audio event detection using semi-supervised learning [39]. In these scenarios, pre-trained models from related domains are used to improve performance on new tasks, leveraging the knowledge learned from the source domain. However, transfer learning can struggle when applied to sonar data, which presents unique acoustic challenges due to the variability in underwater environments, vessel movements, and noise interferences [40]. Models pre-trained on general audio domains may not effectively capture specific complexities when extended to sonar signals [35], [39]. Additionally, transfer learning's ability to generalize varies significantly across different data modalities [41], and the acoustic patterns in sonar data are different from those found in speech or environmental sounds. This can lead to poor generalization when models trained on unrelated datasets are applied to sonar classification tasks. Additionally, underwater conditions, such as salinity, depth, and temperature, introduce variability, making it difficult to find suitable source domains for transfer learning.

Knowledge distillation, on the other hand, aims to create a smaller, more efficient model (student) that can solve the same task as a larger model (teacher) while mitigating performance differences [42]. Instead of relying on pre-trained models from unrelated domains, knowledge distillation involves first training a large, task-specific model (teacher) on the same sonar dataset [38]. The trained teacher model then transfers its learned knowledge to a smaller student model, enabling the student to perform the task with a similar level of accuracy but with reduced computational resources [43], [19]. In contrast to transfer learning, knowledge distillation focuses on compressing the knowledge of a large model into a smaller one for the same task as opposed to only transferring knowledge from a previous tasks while retaining a (usually) larger model. This makes knowledge distillation particularly suited to sonar classification, where training a domain-specific model is essential for capturing unique data characteristics.

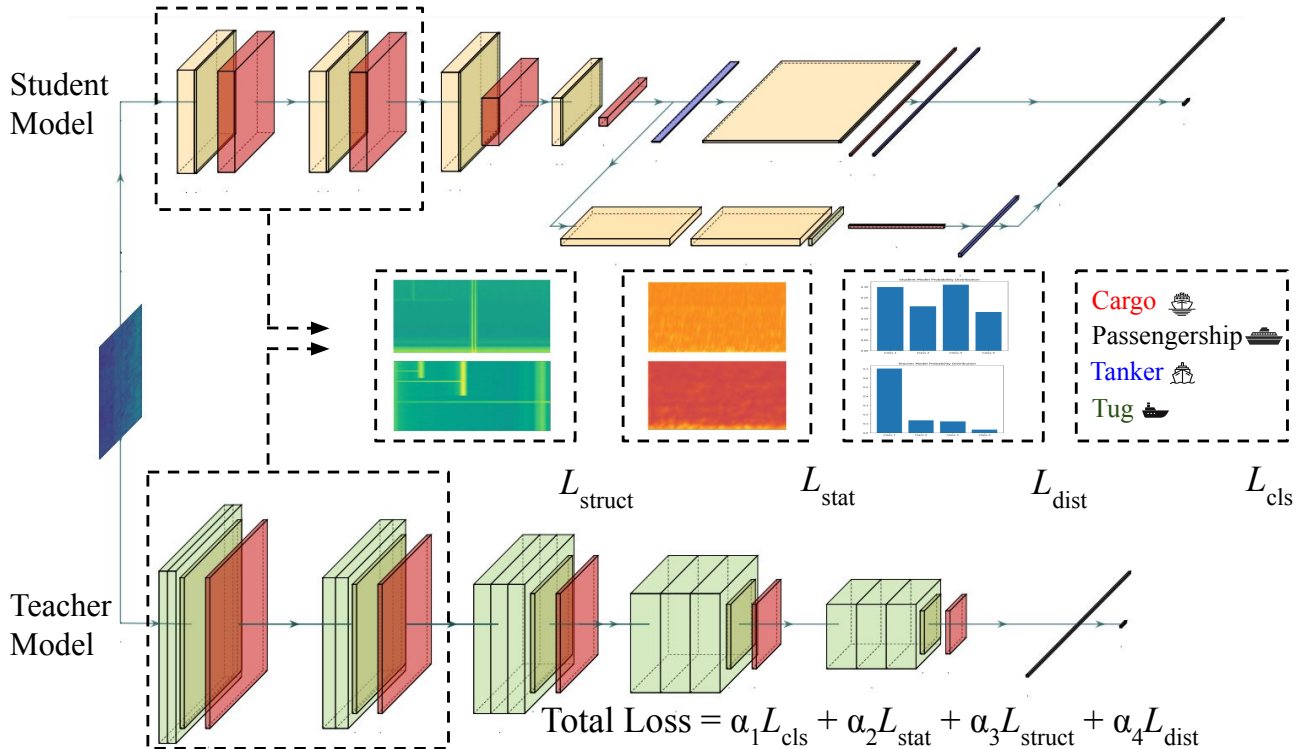


Fig. 1: Overview of the proposed SSATKD framework. The upper network represents the student model, a Histogram Layer Time Delay Neural Network (HLTDNN) adopted from the original HLTDNN paper [44]. The framework is designed to be flexible, accommodating any combination of student and teacher models. In this work, the student model is fixed as the HLTDNN, with the teacher model presented as a general structure that can be any of the following pre-trained audio neural network (PANN) model architectures: CNN14, ResNet38, or MobileNetV1. Each convolutional layer is followed by an activation and pooling layer. The yellow convolutional layers represent the student’s layers, while the green convolutional layers represent the teacher’s layers. In addition to response-based knowledge distillation, SSATKD incorporates feature-based distillation by extracting texture knowledge from low-level features. Specifically, statistical and structural textures are extracted after the second layer of both the teacher and student models. The total loss is calculated as a weighted sum of classification, statistical, structural, and distillation losses.

### III. METHODOLOGY

The proposed SSATKD framework is illustrated in Figure 1. Initially, the input signals are transformed into time-frequency representations, which are then passed into the SSATKD network. The framework focuses on extracting both structural and statistical texture features from the first two layers of the teacher and student models, leveraging the fact that early layers of neural networks capture distinct texture information [45]. Following the distillation approach from [10], the teacher and student networks are aligned by minimizing a combination of response-based and feature-based losses. This alignment ensures the student model effectively learns both high-level semantic information and low-level texture details from the teacher. For statistical texture module, building upon previous research by Zhu et al. [46], the quantization and count operator (QCO) methodology is refined by replacing their linear binning function with radial basis functions (RBFs) for smoother quantization [44]. For the structural texture module, a novel Edge Detection Module is introduced, combining hierarchical decomposition techniques, including the Laplacian Pyramid (LP) and edge detection filters.

#### A. Statistical Texture Module

Statistical textures are first extracted by applying Global Average Pooling (GAP) to the input feature matrix  $\mathbf{A} \in \mathbb{R}^{C \times H \times W}$ , where  $H$  and  $W$  represent the height and width of the feature map, and  $C$  is the number of channels. This operation results in a global averaged feature vector  $\mathbf{g} \in \mathbb{R}^{C \times 1 \times 1}$ , which aggregates information across all spatial dimensions, providing a compact representation of the original feature matrix. Next, the cosine similarity between each spatial position  $\mathbf{A}_{ij}$  (where  $i \in [1, W]$  and  $j \in [1, H]$ ) in the feature map  $\mathbf{A}$  and the global averaged feature vector  $\mathbf{g}$  is computed, resulting in similarity features  $\mathbf{S}$  with dimensions  $1 \times H \times W$ .  $\mathbf{S}$  is then reshaped to  $\mathbf{S} \in \mathbb{R}^{H \times W}$  and quantized into  $Q$  levels, denoted as  $\mathbf{Q} = [Q_1, Q_2, \dots, Q_N]$ . The  $n$ -th quantization level  $Q_n$  is defined in Equation 1:

$$\mathbf{Q}_n = \frac{n}{N}(\max(\mathbf{S}) - \min(\mathbf{S})) + \min(\mathbf{S}), \quad (1)$$

where  $N$  is a hyperparameter for the maximum number of quantization levels, and  $n \in \{1, 2, \dots, N\}$ . To enhance the encoding process by capturing a smoother gradient compared

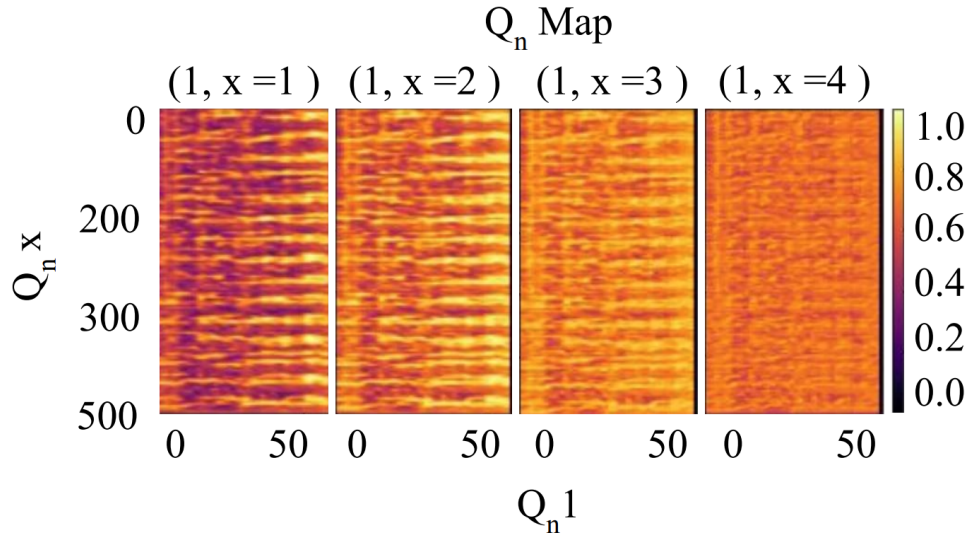


Fig. 2: Visualization of 4 co-occurrence matrices out of the 16 possible matrices, corresponding to a 4-level quantization process. Each matrix captures the pairwise quantization co-occurrence between adjacent spectrogram values in the feature maps. The color intensity represents the frequency of co-occurrence for each pair of quantized levels. Brighter regions (yellow to light green) indicate stronger co-occurrences, while darker regions (dark blue and purple) suggest sparse co-occurrences.

to the linear basis function used in [46], the similarity values are further quantized into  $\mathbf{E}_i \in \mathbb{R}^N$  using an RBF. Here,  $i$  ranges from 1 to  $HW$ , and each dimension  $n \in \{1, 2, \dots, N\}$  of  $\mathbf{E}_i$  is calculated using Equation 2. This quantization process is centered around predefined levels and controlled by the bandwidth parameter  $\gamma$ , set to  $\frac{1}{N/2}$ . This choice of  $\gamma$  ensures effective coverage of the interval between the selected centers  $\mathbf{Q}$ :

$$\mathbf{E}_{i,j} = \exp\left(-\gamma^2 (\mathbf{Q}_n - \mathbf{S}_i)^2\right) \quad (2)$$

The quantized tensor  $\mathbf{E}$  is then reshaped into  $\mathbb{R}^{N \times 1 \times H \times W}$ . For each pair of adjacent spectrogram spectrogram values in the feature map,  $\mathbf{E}_{i,j} \in \mathbb{R}^{N \times 1}$  and  $\mathbf{E}_{i,j+1} \in \mathbb{R}^{N \times 1}$ , their outer product  $\hat{\mathbf{E}}_{i,j}$  is computed to capture adjacent information, as defined in Equation 3:

$$\hat{\mathbf{E}}_{i,j} = \mathbf{E}_{i,j} \times \mathbf{E}_{i,j+1}^T \quad (3)$$

Here,  $T$  denotes the matrix transpose, and  $\times$  represents matrix multiplication. The resulting co-occurrence matrices for adjacent spectrogram cell pairs are visualized in Figure 2, showing how neighboring spectrogram values are correlated. The color scale in the figure ranges from dark purple (representing lower values) to bright yellow (representing higher values). The increasing brightness from the left to right images indicates stronger correlations between adjacent spectrogram cell pairs as moving across the visualizations. This suggests that, in these corresponding regions of  $\mathbf{E}$ , the values of neighboring spectrogram values are becoming more similar.

Subsequently,  $\hat{\mathbf{E}}$  is analyzed to generate a 3-D mapping  $\mathbf{C} \in \mathbb{R}^{N \times N \times 3}$ , where the first two dimensions represent each possible quantization co-occurrence, and the third dimension signifies the corresponding normalized count. This process is described in Equation 4:

$$\mathbf{C} = \text{Concat} \left( \mathbf{Q}, \frac{\sum_{i=1}^H \sum_{j=1}^W \mathbf{E}_{m,n,i,j}}{\sum_{m=1}^N \sum_{n=1}^N \sum_{i=1}^H \sum_{j=1}^W \mathbf{E}_{m,n,i,j}} \right) \quad (4)$$

Here,  $\mathbf{Q} \in \mathbb{R}^{N \times N \times 2}$  represents the pairwise combination of all the quantization levels, where  $\mathbf{Q}_{m,n} = [Q_m, Lv_n]$ . The process is summarized in Algorithm 1, detailing the steps from cosine similarity calculation to generating the final co-occurrence maps.

---

#### Algorithm 1 Statistical Texture Module Processing

---

**Require:** Feature matrix  $\mathbf{A} \in \mathbb{R}^{C \times H \times W}$ , RBF parameter  $\gamma$ , Quantization levels  $N$

- 1: Compute global averaged vector  $\mathbf{g} \in \mathbb{R}^{C \times 1 \times 1}$  from  $\mathbf{A}$
  - 2: Compute cosine similarity matrix  $\mathbf{S} \in \mathbb{R}^{H \times W}$  between  $\mathbf{g}$  and  $\mathbf{A}_{ij}$
  - 3: Quantize  $\mathbf{S}$  into  $N$  levels  $\mathbf{Q} = [Q_1, \dots, Q_N]$
  - 4: Compute RBF-based quantized values  $\mathbf{E} \in \mathbb{R}^{N \times 1 \times H \times W}$
  - 5: Calculate outer product  $\hat{\mathbf{E}}_{ij} = \mathbf{E}_{ij} \times \mathbf{E}_{i,j+1}^T$  for adjacent spectrogram cells
  - 6: Compute co-occurrence map  $\hat{\mathbf{E}} \in \mathbb{R}^{N \times N \times H \times W}$
  - 7: Form 3D map  $\mathbf{C} \in \mathbb{R}^{N \times N \times 3}$
  - 8: **return**  $\mathbf{C}$
- 

#### B. Structural Texture Module

Effective texture representation is critical for texture classification, especially when dealing with challenges such as scale variability and complex textural patterns [47]. In the approach used here, structural texture information in the spectral domain is extracted using a novel edge detection module. This module combines hierarchical decomposition techniques, including the LP and edge detection filters, as illustrated in Figure 3.



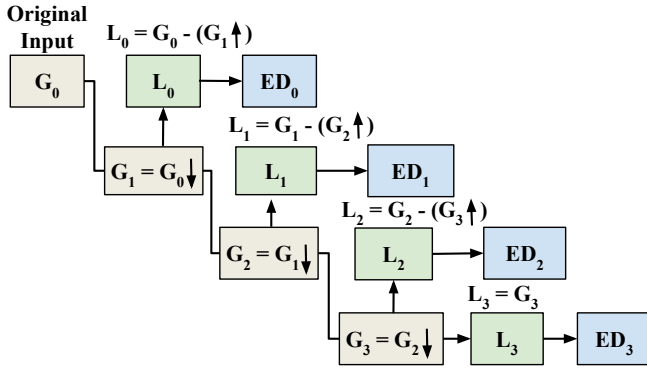


Fig. 3: The steps in the structural module.  $\mathbf{L}_0, \mathbf{L}_1, \mathbf{L}_2, \mathbf{L}_3$  represent the high-pass filtered spectrograms generated by the LP decomposition, while  $\mathbf{G}_0, \mathbf{G}_1, \mathbf{G}_2, \mathbf{G}_3$  correspond to the low-pass filtered spectrograms produced by the Gaussian Pyramid (GP).  $\mathbf{ED}_0, \mathbf{ED}_1, \mathbf{ED}_2, \mathbf{ED}_3$  denote the edge detection filters applied at each level.

---

**Algorithm 2** Structural Texture Module Processing
 

---

**Require:** Feature Map  $I \in \mathbb{R}^{C \times H \times W}$ , Levels  $\mathcal{N}$ , Sobel filters

- 1: **LP Decomposition:**
  - 2: Initialize  $G_0 = I$
  - 3: **for**  $k = 0$  to  $\mathcal{N} - 1$  **do**
  - 4:    $G_{k+1} \leftarrow G_k \downarrow$
  - 5:    $L_k \leftarrow G_k - (G_{k+1} \uparrow)$
  - 6: **end for**
  - 7:  $L_{\mathcal{N}} \leftarrow G_{\mathcal{N}}$  (low-frequency residual)
  - 8: **Edge Detection:**
  - 9: **for each**  $L_k$  **do**
  - 10:   **for each**  $\theta$  in  $\{0^\circ, 45^\circ, \dots, 315^\circ\}$  **do**
  - 11:      $E_k^\theta \leftarrow \text{Sobel}(L_k, \theta)$
  - 12:   **end for**
  - 13: **end for**
  - 14: **Fusion:**
  - 15: **Weighted Sum:** Combine  $E_k^\theta$  via grouped convolution
  - 16: **Max Fusion:**  $E_k \leftarrow \max_\theta(E_k^\theta)$
  - 17: **All Fusion:** Retain all  $E_k^\theta$
  - 18: **return** Final fused structural texture representation
- 

1) *Laplacian Pyramid Decomposition:* LP is a linear and invertible representation that consists of band-pass images derived from a GP, each representing different scales, along with a low-frequency residual [48]. The downsampling operation, denoted as  $\downarrow$ , blurs and reduces the size of a matrix  $\mathbf{I}$ , producing a smaller matrix  $\mathbf{I} \downarrow$  with half the height and width of the original, as shown in Figure 6. Conversely, the upsampling operation, denoted as  $\uparrow$ , smooths and doubles the size of a matrix  $\mathbf{I}$ , resulting in a matrix  $\mathbf{I} \uparrow$  with dimensions twice that of the input.

To construct the GP  $\{\mathbf{G}_0, \mathbf{G}_1, \dots, \mathbf{G}_{\mathcal{N}}\}$ , the downsampling operation is applied iteratively to the original image,  $\mathbf{G}_0 = \mathbf{I}$  iteratively to generate each subsequent level  $\mathbf{G}_k$ . In this case, a 4-level decomposition is used, meaning  $\mathcal{N} = 4$ . The LP  $\{\mathbf{L}_0, \mathbf{L}_1, \dots, \mathbf{L}_{\mathcal{N}-1}\}$  is created by subtracting the upsampled lower-resolution Gaussian level  $\mathbf{G}_{k+1} \uparrow$  from the current level

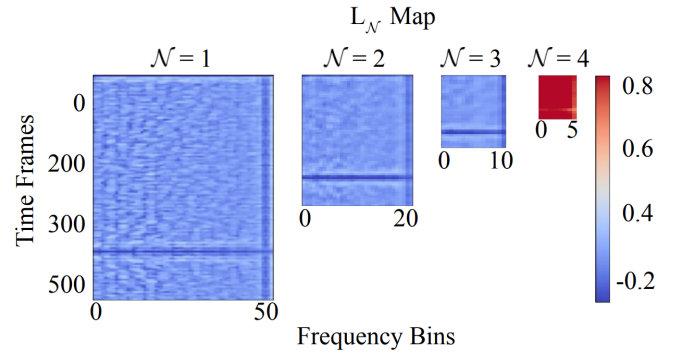


Fig. 4: Visualization of the 4-level LP decomposition stages. This figure illustrates the downsampling process that generates multi-scale Gaussian levels, with the LP capturing the differences between these levels. The decomposition preserves fine details across different scales, highlighting the transitions from finer to coarser resolutions.

$\mathbf{G}_k$ , as defined in Equation 5:

$$\mathbf{L}_k = \mathbf{G}_k - (\mathbf{G}_{k+1} \uparrow) \quad (5)$$

Each level  $\mathbf{L}_k$  captures details at a specific scale, while the final level  $\mathbf{L}_{\mathcal{N}}$  represents the low-frequency residual, equivalent to the last level of the GP,  $\mathbf{G}_{\mathcal{N}}$ . To reconstruct the original image from the LP, the process is reversed, as shown in Equation 6:

$$\mathbf{G}_k = \mathbf{L}_k + (\mathbf{G}_{k+1} \uparrow) \quad (6)$$

The reconstruction process begins with  $\mathbf{G}_{\mathcal{N}} = \mathbf{L}_{\mathcal{N}}$  and proceeds by upsampling and adding the difference matrices from finer levels until the full-resolution image  $\mathbf{G}_0$  is restored. This process is visualized in Figure 4.

2) *Edge Detection Filters and Edge Responses:* At each level of the LP, directional information is captured using edge detection filters. Specifically, Sobel kernels [49] are applied to the feature maps at each level to generate edge responses across eight orientations: 0, 45, 90, 135, 180, 225, 270, and 315 degrees. These edge responses emphasize the directional texture patterns, which are crucial for robust texture representation. To aggregate these edge responses, three distinct fusion methods are implemented:

- **Weighted Sum:** A grouped convolution combines responses, learning their relative importance.
- **Max:** The strongest edge response is retained by selecting the maximum value across channels.
- **All:** All edge responses are retained, preserving full directional information.

### C. Loss Functions in SSTAKD

Distinct loss functions are adopted to balance the objectives of texture analysis and classification.

1) *Statistical Loss:* The three-dimensional feature maps  $\mathbf{C} \in \mathbb{R}^{N \times N \times 3}$  generated by the statistical module represent co-occurrence matrices and counts derived from both the teacher and student models. These feature maps capture the distributional characteristics of the models. Since the teacher

and student models may have different bin centers and widths for their histograms, direct comparison of their distributions can be challenging. To address this, a 2D histogram-based EMD loss is implemented, which involves computing histograms for both models and using EMD to ensure a fair comparison. First, the 2D histograms for the teacher  $\mathbf{H}_T$  and student  $\mathbf{H}_S$  models are calculated. These histograms are then normalized to sum to one to form valid probability mass functions.

Next, the cumulative distribution functions (CDFs) for each histogram are calculated by summing the normalized values along both dimensions, as given by Equation 7:

$$\begin{aligned} \text{CDF}_T(x_T, y_T) &= \sum_{i \leq x_T} \sum_{j \leq y_T} \mathbf{H}_T(i, j) \\ \text{CDF}_S(x_S, y_S) &= \sum_{i \leq x_S} \sum_{j \leq y_S} \mathbf{H}_S(i, j) \end{aligned} \quad (7)$$

Here,  $x_T$  and  $y_T$  represent the coordinates in the teacher model's histogram, while  $x_S$  and  $y_S$  represent the coordinates in the student model's histogram.

The ground matrix  $\mathbf{D}$  is then computed using the Euclidean distances between each pair of 2D bin centers to quantify the differences between the histograms.  $\mathbf{D}$  represents the cost of transferring knowledge from the teacher to the student, as defined in Equation 8:

$$\mathbf{D} = \sqrt{(x_T - x_S)^2 + (y_T - y_S)^2} \quad (8)$$

Finally, the statistical loss  $L_{\text{stat}}$  is defined as the 2D EMD, computed by summing the weighted squared difference between the CDFs of the teacher and student histograms, as shown in Equation 9:

$$L_{\text{stat}} = \sum_{x_T, y_T} \sum_{x_S, y_S} \mathbf{D} \cdot (\text{CDF}_T(x_T, y_T) - \text{CDF}_S(x_S, y_S))^2 \quad (9)$$

2) *Structural Loss*: To quantify the alignment between structural features, the structural loss  $L_{\text{struct}}$  is defined using cosine similarity. Cosine similarity measures the angle between two vectors, focusing on their directional alignment rather than their magnitude, resulting in an effective metric for comparing structural patterns in the feature space. The objective is to minimize the discrepancy between the structural features of the teacher and student models. Given the feature maps  $\mathbf{F} \in \mathbb{R}^{C \times H \times W}$ , the cosine similarity is calculated along the feature dimension. Thus, the structural loss  $L_{\text{struct}}$  is formulated as Equation 10:

$$L_{\text{struct}} = 1 - \text{CosSim}(\mathbf{F}_i^{\text{struct};T}, \mathbf{F}_i^{\text{struct};S}) \quad (10)$$

Here,  $\mathbf{F}_i^{\text{struct};T}$  and  $\mathbf{F}_i^{\text{struct};S}$  represent the structural feature maps of the teacher and student models for the  $i$ -th sample, and the cosine similarity is computed along the channel dimension  $C$ .

3) *Classification Loss*: Cross-entropy loss is used to measure the alignment between predicted probabilities and true class labels, as defined in Equation 11:

$$L_{\text{cls}} = - \sum_{i=1}^C y_i \log(p_i) \quad (11)$$

where  $p$  represents the predicted probability distribution,  $y$  is the one-hot encoded true labels, and  $C$  is the number of classes.

4) *Distillation Loss*: To promote response-based knowledge distillation and enable the student network to approximate the soft targets from the teacher network, EMD loss is employed. The bin centers and widths for the distillation loss are identical for both the student and teacher models, as they represent the softmax logits from each network, which correspond to the probability distribution over the classes. EMD is well-suited for scenarios where the teacher and student models have differing architectures, making direct layer-to-layer mappings infeasible [50]. EMD quantifies the dissimilarity between probability distributions by calculating the minimum cost required to transform one distribution into another. The distillation loss,  $L_{\text{distill}}$ , is defined in Equation 12 as the mean squared difference between the CDFs of the student and teacher models:

$$L_{\text{distill}} = \frac{1}{C} \sum_{i=1}^C (\text{CDF}_{\text{student}}(i) - \text{CDF}_{\text{teacher}}(i))^2 \quad (12)$$

where  $i$  refers to the class index within the CDFs, and  $C$  is the number of classes. The sum computes the squared difference between the CDFs of the student and teacher models across  $C$  classes for a single sample.

#### D. Overall Objective Function

Achieving the right balance among objectives is crucial for maximizing the model's overall performance. To achieve this balance, an uncertainty-based loss weighting approach [3] is utilized. This method dynamically adjusts the contribution of each loss component based on the uncertainty of the corresponding task. The total loss for the SSATKD model is therefore computed using Equation 13:

$$\text{Total Loss} = \alpha_1 \cdot L_{\text{cls}} + \alpha_2 \cdot L_{\text{stat}} + \alpha_3 \cdot L_{\text{struct}} + \alpha_4 \cdot L_{\text{dist}} \quad (13)$$

where  $\alpha_1$ ,  $\alpha_2$ ,  $\alpha_3$ , and  $\alpha_4$  are the weights assigned to each loss component. These weights are determined based on the variance of each task's predictions, which reflects the uncertainty in the model's performance for that task. The weights are computed using Equation 14:

$$\alpha_i = \frac{1}{\sigma_{L_i}^2} + \log(\sigma_{L_i}^2) \quad (14)$$

In this equation,  $\sigma_{L_i}^2$  represents the variance associated with the  $i$ -th task's loss component, with higher variance indicating greater uncertainty. By scaling  $\alpha_i$  inversely with the precision (the inverse of the variance), the model places more importance on tasks where it has higher confidence and reduces the influence of tasks with greater uncertainty. This uncertainty-based weighting approach eliminates the need for manual tuning of loss weights, allowing the model to automatically balance the different loss components for optimal performance.

TABLE I: Overall baseline performance metrics for the student model HLTDNN and the teacher models. The teacher models in this study include three PANN models: CNN14, ResNet38, and MobileNetV1. The metrics reported include accuracy, precision, recall, F1-score, and the number of parameters for each model. The best average metric for each category is bolded. Each metric represents the average score across three experimental runs with random initialization, along with one standard deviation ( $\pm 1\sigma$ ).

Baseline	Model Name	Accuracy	Precision	Recall	F1-score	Parameters
Student Model	HLTDNN	59.62 $\pm$ 1.69%	64.07 $\pm$ 1.24%	60.14 $\pm$ 1.46%	59.24 $\pm$ 2.04%	11.3 K
Teacher Model	CNN14	<b>71.33 <math>\pm</math> 1.21%</b>	<b>74.41 <math>\pm</math> 1.35%</b>	<b>71.87 <math>\pm</math> 1.26%</b>	<b>71.25 <math>\pm</math> 1.27%</b>	79.7 M
	ResNet38	64.93 $\pm$ 1.52%	68.98 $\pm$ 1.23%	65.13 $\pm$ 1.35%	64.74 $\pm$ 2.01%	72.7 M
	MobileNetV1	66.64 $\pm$ 1.92%	69.89 $\pm$ 1.78%	66.74 $\pm$ 1.71%	66.69 $\pm$ 1.95%	4.3 M

## IV. EXPERIMENTAL SETUP

### A. Data Preparation

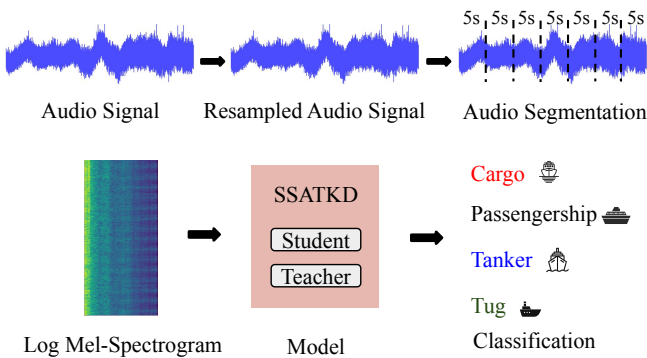


Fig. 5: Data preparation pipeline for the SSATKD framework. The process includes resampling original audio signals from the DeepShip dataset to 32 kHz, segmenting the signals into 5-second intervals, transforming the segments into log Mel-frequency spectrograms. These spectrograms are used as input for the SSATKD framework.

For all experiments in this study, the DeepShip dataset [51] was used. This dataset contains 609 recordings of underwater acoustic signals representing four different ship types: cargo, passenger ship, tanker, and tug. To ensure compatibility with the pretraining configuration of the PANN teacher models, all signals were resampled to a frequency of 32 kHz. Each resampled signal was then segmented into five-second intervals. The dataset was split into 70% training, 10% validation, and 20% testing based on the signal origin, ensuring that all segments of each signal remained in the same partition to prevent data leakage. Each five-second segment was transformed into a log Mel-frequency spectrogram with a Hann window of size 1024, a hop length of 320, and 64 mel filters. Following [52], SpecAugmentation [53] was applied to the spectrograms to enhance model robustness to data variations. This augmentation technique introduces transformations such as time masking and frequency masking, which randomly conceal portions of the spectrogram, forcing the model to rely on the remaining visible information, thus improving generalization. These spectrograms serve as input to the SSATKD framework. The entire data preparation pipeline is illustrated in Figure 5.

### B. Implementation Details

The HLTDNN model is fixed as the student model in all experiments. For the teacher model, three different PANN models are evaluated [52]: CNN14, ResNet38 and MobileNetV1. These models were selected because they were the top three highest-performing models in the original PANN paper, making them strong candidates for the knowledge distillation experiments. To ensure robustness, each model was tested across three separate runs with different random initializations. The AdamW optimizer was used with initial learning rate of 0.0001, which was adjusted using a learning rate schedule given by  $\text{lr} \times \left(1 - \frac{\text{iter}}{\text{max\_iter}}\right)^{0.9}$ . All models were trained for a total of 150 epochs, with an early stopping patience set to 50 epochs. A batch size of 32 was used throughout the training.

## V. RESULTS AND DISCUSSION

### A. Baseline Classification Performance

The metrics presented in Table I offer a comprehensive comparison between independently trained models: the baseline student model HLTDNN, and the teacher models CNN14, ResNet38, and MobileNetV1. The HLTDNN student model, with its lightweight architecture consisting of only 11.3K parameters, achieved an accuracy of 59.62%. While this performance is lower than that of the teacher models, it reflects a balance between model simplicity and computational efficiency. HLTDNN's compact size makes it a suitable candidate for resource-constrained environments. Among the teacher models, CNN14 showed the best overall performance, achieving an accuracy of 71.33%. This high accuracy can be attributed to its large parameter count of 79.7M, which enables more complex feature extraction. Additionally, CNN14's precision, recall, and F1-score also reflect robust performance, making CNN14 the most effective teacher model in this study.

ResNet38, with 72.7M parameters, achieved an accuracy of 64.93%, which, while better than the student model, is lower than CNN14. This suggests that although ResNet38 benefits from a large parameter size, it may not be as optimized as CNN14 for this specific task. MobileNetV1, with 4.3M parameters, presents a compelling trade-off between efficiency and performance. MobileNetV1 achieved an accuracy of 66.64%, outperforming ResNet38 despite having significantly fewer parameters. This indicates that MobileNetV1 is more efficient in terms of parameter utilization, providing competitive performance with far fewer resources. Overall, the results highlight the expected trade-offs: larger models such as

TABLE II: Overall performance metrics for knowledge distillation using the SSATKD framework, with evaluation of the combination of three different teacher models (CNN14, ResNet38, and MobileNetV1) with the HLTDDN student model. The average score within one standard deviation ( $\pm 1\sigma$ ) across the three experimental runs of random initialization is shown. Metrics include accuracy, precision, recall, F1-score, and the number of parameters. The best average metric is bolded.

SSATKD Models	Accuracy	Precision	Recall	F1-score	Parameters
CNN14_HLTDDN	64.72 $\pm$ 1.92%	<b>70.01 <math>\pm</math> 0.29%</b>	64.93 $\pm$ 1.52%	64.61 $\pm$ 2.15%	12.3 K
ResNet38_HLTDDN	65.62 $\pm$ 1.75%	70.01 $\pm$ 1.24%	65.62 $\pm$ 1.75%	66.41 $\pm$ 1.34%	12.3 K
MobileNetV1_HLTDDN	<b>66.22 <math>\pm</math> 0.83%</b>	68.94 $\pm$ 1.14%	<b>67.21 <math>\pm</math> 0.12%</b>	<b>65.75 <math>\pm</math> 0.94%</b>	12.3 K

CNN14 offer superior performance at the cost of high computational complexity, while smaller models like HLTDDN and MobileNetV1, strike a balance between performance and efficiency, making them appealing choices for scenarios where resources are limited.

### B. SSATKD Classification Performance

Table II summarizes the performance metrics for knowledge distillation using the SSATKD framework, comparing the impact of different teacher models (CNN14, ResNet38, and MobileNetV1) on the HLTDDN student model’s performance. While all teacher models improved the student’s performance, certain trends stand out. The highest test accuracy, 66.22%, was achieved by the MobileNetV1\_HLTDDN combination, suggesting that MobileNetV1, despite its smaller architecture and fewer parameters, transferred knowledge more effectively compared to the larger models. The F1-score of 65.75% further confirms MobileNetV1’s balance between precision and recall, making it an efficient choice for knowledge distillation.

The ResNet38\_HLTDDN combination followed closely, achieving an accuracy of 65.62% and an F1-score of 65.31%. ResNet38 displayed a consistent balance between precision (70.01%) and recall (65.62%), offering reliable performance across multiple metrics. In contrast, the CNN14\_HLTDDN combination, while still beneficial, showed the lowest accuracy (64.72%) and an F1-score of 64.61%, indicating that the knowledge transfer process from CNN14 was less effective.

After applying SSATKD, the HLTDDN student model’s size increased from 11.3K to 12.3K parameters due to a 1x1 convolution layer introduced to align feature sizes between the teacher and student models. Despite this minimal increase in model size, there was a significant boost in performance when compared to the baseline HLTDDN model.

Among all combinations, MobileNetV1\_HLTDDN proved to be the most effective, offering a balance of high accuracy and model efficiency. ResNet38 provided a consistent balance between precision, while CNN14, despite being a strong standalone model, was less effective in transferring knowledge in the distillation setting. These results highlight the versatility of the SSATKD framework in enhancing lightweight student models in a resource-efficient manner. Therefore, the MobileNetV1\_HLTDDN combination was chosen for further ablation studies, as it offers the best trade-off between performance and model efficiency.

Confusion matrices for the baseline HLTDDN and SSATKD HLTDDN using the MobileNetV1\_HLTDDN combination are displayed in Figures 6a and 6b, respectively. In the baseline

model, there is significant confusion between similar classes, such as Cargo and Tanker. For example, only 47.95% of Cargo samples are correctly classified, with 36.77% misclassified as Tanker. Tug also shows major misclassification as Passengership, with only 26.85% correctly classified and 40.08% misclassified.

After applying SSATKD, classification performance improves across all categories. Cargo’s correct classification increases to 62.28%, with a reduction in misclassification with Tanker (down to 23.81%). Tug shows the most substantial improvement, with correct classification rising from 26.85% to 76.72%, significantly reducing confusion with Passengership. These results demonstrate SSATKD’s ability to better distinguish acoustically similar classes. Overall, SSATKD increases test accuracy from 59.62% to 66.22%, with reduced classification errors and tighter standard deviations. The SSATKD framework enhances both precision and recall, particularly for challenging classes, without significantly increasing model complexity. This highlights the effectiveness of texture-based knowledge distillation in improving model performance for underwater acoustic signals.

### C. Ablation study

#### 1) Analysis of the temperature parameter tuning method:

The temperature parameter in knowledge distillation plays a crucial role in controlling the softness of the softmax probabilities produced by the teacher model. Higher temperatures smooth the probability distribution, making it easier for the student model to learn from the teacher’s outputs. During backpropagation, the temperature parameter can either be fixed or learned, meaning it gets updated along with the model’s parameters. The choice of temperature value significantly impacts the distillation process, with typical values like 1 and 2 representing the initial settings for softening the logits. The results in Table III show that different temperature tuning

TABLE III: Comparison of different distillation temperature tuning methods on model accuracy. Results show the impact of fixed and learnable temperature approaches. The highest accuracy, highlighted in bold, was achieved using the ‘Learnable - Initialized with 1’ method.

Tuning Method	Accuracy
Fixed to 1	64.99 $\pm$ 0.77%
Fixed to 2	65.87 $\pm$ 1.91%
Learnable - Initialized with 1	<b>65.87 <math>\pm</math> 1.26%</b>
Learnable - Initialized with 2	60.27 $\pm$ 9.58%
Learnable - Sharpness Based	61.36 $\pm$ 4.19%



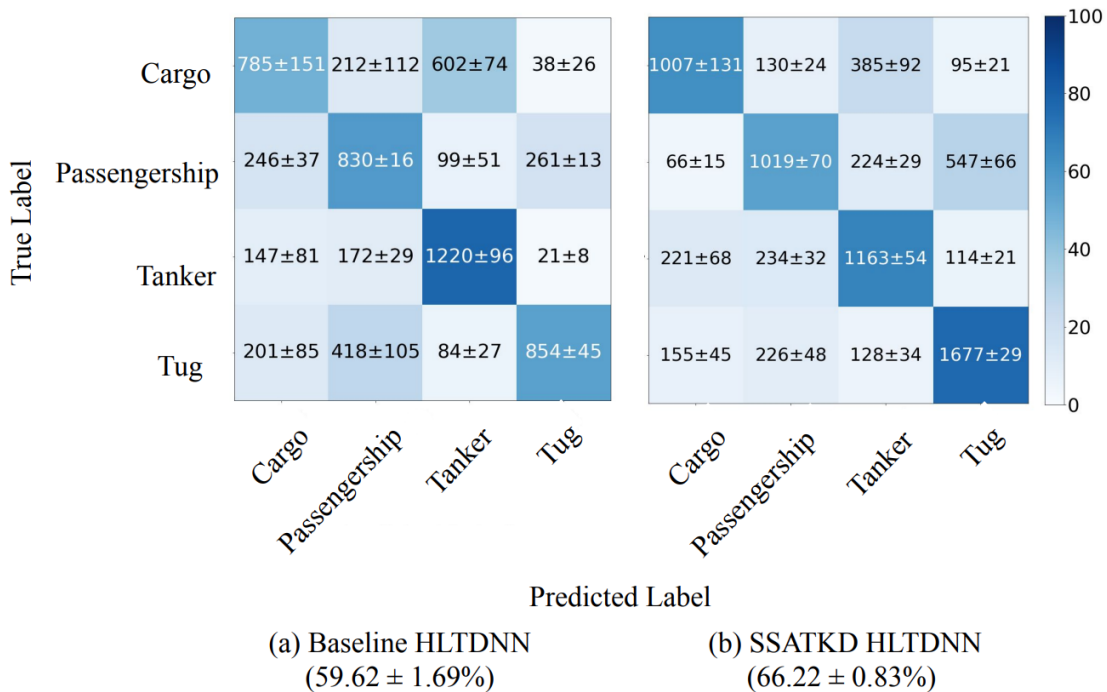


Fig. 6: Average confusion matrices for the HLTDDN model comparing:(a) Baseline HLTDDN and (b) SSATKD HLTDDN after applying SSATKD. Each cell displays the mean and standard deviation of the predicted class samples. The SSATKD approach significantly enhances classification performance, resulting in a notable accuracy improvement from 59.62% to 66.22%, demonstrating the effectiveness of distilling texture-based knowledge.

methods yield varying accuracy in the knowledge distillation process. Both fixed values, “Fixed to 1” and “Fixed to 2,” perform similarly well, with “Fixed to 2” achieving the highest accuracy at 65.87%.

Among the learnable methods, “Learnable - Initialized with 1” also performed comparably, indicating that initializing the temperature to 1 is a robust approach. However, initializing with 2 led to significant accuracy fluctuations ( $60.27\% \pm 9.58\%$ ), likely due to instability in the model. The sharpness-based method [54] achieved moderate results (61.36%) but displayed higher variance, suggesting room for further refinement. In summary, fixed values or carefully initialized learnable temperatures provide stable and competitive performance.

TABLE IV: Effect of statistical, structural, and distillation loss combinations on model accuracy. The table illustrates how different combinations of loss components influence model performance, highlighting the contribution of each component. The highest accuracy, highlighted in bold, was achieved by combining structural and distillation loss without the statistical loss.

Statistical	Structural	Distillation	Accuracy
			59.62 ± 0.02%
		✓	65.99 ± 0.59%
	✓		65.80 ± 0.52%
	✓	✓	<b>67.46 ± 0.91%</b>
✓			65.43 ± 0.60%
✓		✓	61.85 ± 0.52%
✓	✓		64.84 ± 1.45%
✓	✓	✓	66.22 ± 0.83%

2) *Analysis of loss components*: Table IV presents the impact of various combinations of structural, statistical, and distillation loss terms on the accuracy of the HLTDDN student model, with classification loss applied in all cases. The baseline accuracy with only classification loss is 59.62%. Incorporating the distillation loss alone boosts performance to 65.99%, highlighting the advantage of knowledge transfer from the teacher model. Similarly, the addition of statistical loss alone increases accuracy to 65.80%, indicating that statistical alignment also contributes positively to performance. However, combining both statistical and distillation losses results in a decrease to 61.85%, suggesting possible interference between these two losses when applied together.

When the structural loss is combined with classification loss, the accuracy improves to 65.43%. The combination of structural and distillation losses achieves the highest accuracy of 67.46%, showing the strong interaction between these losses. The pairing of structural and statistical losses results in a slightly lower accuracy of 64.84%. Lastly, applying all three losses together produces an accuracy of 66.22%. The results show that each loss term helps improve accuracy on its own. However, when combined, certain combinations work better than others. The structural and distillation losses together led to the biggest improvement whereas the statistical and distillation losses together reduced accuracy. This drop in performance may be due to the equal bin size configuration to learn the statistical textures of the data. By using leveraging learnable bin centers and widths via backpropagation [49], future experiments could potentially improve performance with minimal overhead.

3) *Analysis of Structural Module*: Table V presents the performance of different fusion modes in the structural module. The “All Fusion” method achieved the highest accuracy of 66.22%, demonstrating the effectiveness of retaining all edge responses from different orientations to capture comprehensive texture information. The “Max Fusion” method, which selects the strongest edges, reached 65.38%, but may have missed some finer details. The “Weighted Sum Fusion” method resulted in 61.77%, likely due to potential loss of directional information during linear combination. Overall, the “All Fusion” method provided the best balance between accuracy and model complexity.

TABLE V: Impact of different fusion modes on test accuracy and model parameters. The highest accuracy, highlighted in bold, was achieved using the “All Fusion” mode.

Fusion Mode	Accuracy	Params
All	<b>66.22 ± 0.83%</b>	12.3 K
Max	65.38 ± 0.58%	12.3 K
Weighted Sum	61.77 ± 1.21%	14.6 K

Table VI shows the impact of decomposition levels. A 4-level decomposition produced the best results with 66.22%, while using fewer (2 levels) led to slightly lower accuracy (64.82%). Increasing to 8 levels reduced accuracy to 61.77%, likely due to overfitting or unnecessary complexity. This suggests that while multi-level decomposition captures valuable structural details, there is an optimal balance between complexity and performance, with 4 levels proving to be the most effective in the case of these experiments.

TABLE VI: Effect of decomposition levels on model accuracy. The highest accuracy, highlighted in bold, was achieved at 4 decomposition levels.

Decomposition Levels	Accuracy
2	64.82 ± 0.28%
4	<b>66.22 ± 0.83%</b>
8	61.77 ± 1.21%

4) *Analysis of Statistical Module*: Table VII compares the performance of Linear and RBF quantization methods. RBF quantization outperformed Linear, achieving 65.87% accuracy compared to 61.77%. This suggests that RBF provides a smoother and more precise representation, whereas the simpler Linear method is less effective at handling finer details in the data.

TABLE VII: Effect of binning methods on model accuracy. The highest accuracy, highlighted in bold, was achieved using the RBF binning method.

Binning Method	Accuracy
Linear	61.77 ± 1.42%
RBF	<b>65.87 ± 1.26%</b>

Table VIII shows the impact of the number of quantization levels. Accuracy peaks at 66.22% with 4 levels, indicating that a moderate level of quantization effectively captures essential details. Increasing the levels to 16 and 32 leads to a performance drop, likely due to overfitting or sensitivity

to minor variations. Thus, while finer quantization helps, too many levels can degrade performance.

TABLE VIII: Effect of quantization levels and bins on model accuracy. The highest accuracy, highlighted in bold, was achieved using 4 quantization levels.

Number of Levels/Bins	Accuracy
2	61.83 ± 6.71%
4	<b>66.22 ± 0.83%</b>
8	65.87 ± 1.26%
16	61.84 ± 2.15%
32	43.45 ± 5.13%

D. *Comparison with Existing State-of-the-Art Knowledge Distillation Methods*

The proposed SSATKD was compared against five state-of-the-art knowledge distillation methods: Semantic Representational Distillation (SRD) [55], Teacher-Free Knowledge Distillation (TF-KD) [56], Contrastive Representation Distillation (CRD) [57], Prime-Aware Adaptive Distillation (PAD) [58], and Correlation Congruence for Knowledge Distillation (CCKD) [59]. These methods were selected based on their recent implementation in the `torchdistill` framework [60], which provides a robust and up-to-date benchmark for a fair evaluation. Each method uses the same teacher-student configuration: MobileNetV1 as the teacher and HLTDDN as the student, trained on the DeepShip dataset, ensuring consistency in model pairing across comparisons. SSATKD was also re-evaluated within the `torchdistill` framework to maintain identical training conditions. The results of this comparison are summarized in Table IX, which shows performance across metrics of accuracy, precision, recall, and F1-score. As shown, SSATKD demonstrates better performance across all metrics, demonstrating the proposed method’s effectiveness relative to existing methods.

TABLE IX: Performance comparison of SSATKD with various knowledge distillation methods using the `torchdistill` framework [60] on the Deepship dataset. Metrics include accuracy, precision, recall, and F1-score, averaged over three runs, with best performances in bold.

Method	Accuracy	Precision	Recall	F1-score
SRD [55]	61.99 ± 1.52%	62.50 ± 1.64%	62.32 ± 1.66%	61.93 ± 1.82%
TF-KD [56]	60.33 ± 1.72%	60.51 ± 1.10%	59.54 ± 1.31%	60.23 ± 1.02%
CRD [57]	61.42 ± 1.87%	63.33 ± 1.41%	60.82 ± 1.92%	62.12 ± 1.77%
PAD [58]	52.25 ± 1.33%	53.54 ± 1.27%	52.77 ± 1.26%	52.53 ± 1.22%
CCKD [59]	60.13 ± 1.68%	60.54 ± 1.81%	58.45 ± 1.12%	60.73 ± 1.42%
SSATKD (Ours)	<b>65.92 ± 1.18%</b>	<b>67.65 ± 1.21%</b>	<b>66.32 ± 0.88%</b>	<b>67.18 ± 1.22%</b>

SSATKD’s advantages compared to the other methods can be attributed to the unique approach of combining texture modeling and diversity preservation, both of which significantly enhance the student model’s capacity for learning detailed and comprehensive representations.

When compared to SRD, which focuses on aligning individual semantic representations between teacher and student models, SSATKD directly captures relationships between features across multiple scales (structural texture features). SRD’s individual feature alignment lacks the ability to represent

complex, high-dimensional dependencies, limiting the richness of the student model’s learned features [61]. SSATKD’s EDM preserves information across different feature levels, enabling the student model to incorporate the spatial context present in the teacher model.

TF-KD, while effective in scenarios without a teacher, does not benefit from the structured knowledge transfer that comes from a pre-trained teacher model. By avoiding reliance on a teacher, TF-KD loses the advantage of explicitly transferring the structural and statistical knowledge embedded within a trained network. In contrast, SSATKD uses the teacher model to transfer both low-level structural information through the edge detection strategy and statistical measurements through texture quantization, resulting in a more comprehensive knowledge transfer.

CRD relies on maximizing mutual information between teacher and student representations, effectively capturing relational information. However, contrastive learning often demands large batch sizes and extensive training to be effective [62]. Additionally, CRD’s focus on transferring structural knowledge between the student and teacher. SSATKD not only models structural texture information, but also statistical texture through the RBF quantization, which enables the student model to learn additional feature representations that can improve performance.

PAD prioritizes prime samples based on data uncertainty, assigning higher importance to samples with low uncertainty during training. However, this selective weighting can reduce generalizability because it biases the model towards certain types of data, potentially overlooking rarer or more complex patterns in less prioritized samples, which are equally important for robust generalization across diverse datasets [63]. By emphasizing only “prime” samples, PAD risks training the model on a narrow representation, making it less effective on broader, unseen data. In contrast, SSATKD uses a systematic approach to retain both low-level structural and statistical feature across all samples, allowing the student model to learn from a more comprehensive set of features.

Finally, CCKD aims to align relational information between teacher and student models, capturing some degree of inter-channel correlation. However, CCKD lacks a holistic approach to preserve feature diversity, which is essential for effective data representations [64]. SSATKD improves on this by explicitly modeling inter-channel correlations across multiple orientations and scales, and by preserving feature diversity through the statistical texture module. These strategies allow SSATKD to capture a more comprehensive range of relational and structural information, leading to consistently higher performance across all metrics.

## VI. CONCLUSION

This work introduced the SSATKD framework, designed to improve passive sonar target classification by distilling both low-level texture features and high-level responses from teacher models into a student model. The experimental results demonstrated that the framework achieves maximal performance when combining both distillation and structural losses,

emphasizing the importance of direct knowledge transfer through feature-based and knowledge-response-based distillation.

Within the statistical module, RBF quantization was shown to outperform linear quantization, proving effective in capturing subtle feature variations learned by the network. An optimal quantization level of 4 was identified, balancing feature representation and efficiency. While the incorporation of structural and statistical losses provided some improvements, their contributions were secondary to response-based distillation, emphasizing the dominant role of knowledge transfer in the SSATKD framework. Furthermore, SSATKD has been compared with other existing knowledge distillation methods, demonstrating improved results through a unique approach that combines texture feature-based distillation with response-based distillation. By incorporating both structural and statistical texture information, SSATKD transfers a richer set of features to the student model, enabling more robust and accurate learning.

Future work could focus on further refining the balance of the loss components to improve performance. Beyond passive sonar classification, the SSATKD framework could be extended to other domains of audio classification, such as environmental sound recognition or bioacoustics, offering a broader impact. Integrating techniques like self-supervised learning or multi-modal fusion could also open up new possibilities for improving the model’s generalization and efficiency.

## REFERENCES

- [1] K. Xu, Q. Xu, K. You, B. Zhu, M. Feng, D. Feng, and B. Liu, “Self-supervised learning-based underwater acoustical signal classification via mask modeling,” *The Journal of the Acoustical Society of America*, vol. 154, no. 1, pp. 5–15, 2023.
- [2] S. Wang and X. Zeng, “Robust underwater noise targets classification using auditory inspired time–frequency analysis,” *Applied Acoustics*, vol. 78, pp. 68–76, 2014.
- [3] A. Kendall, Y. Gal, and R. Cipolla, “Multi-task learning using uncertainty to weigh losses for scene geometry and semantics,” in *Proceedings of the IEEE conference on computer vision and pattern recognition*, 2018, pp. 7482–7491.
- [4] Z. Lian, K. Xu, J. Wan, and G. Li, “Underwater acoustic target classification based on modified gfcc features,” in *2017 IEEE 2nd Advanced Information Technology, Electronic and Automation Control Conference (IAEAC)*. IEEE, 2017, pp. 258–262.
- [5] J. Ghosh, K. Turner, S. Beck, and L. Deuser, “Integration of neural classifiers for passive sonar signals,” in *Control and Dynamic Systems*. Elsevier, 1996, vol. 77, pp. 301–338.
- [6] D. Neupane and J. Seok, “A review on deep learning-based approaches for automatic sonar target recognition,” *Electronics*, vol. 9, no. 11, p. 1972, 2020.
- [7] G. Li, W. Bu, and H. Yang, “Noise reduction method for ship radiated noise signal based on modified uniform phase empirical mode decomposition,” *Measurement*, vol. 227, p. 114193, 2024.
- [8] X. Luo, L. Chen, H. Zhou, and H. Cao, “A survey of underwater acoustic target recognition methods based on machine learning,” *Journal of Marine Science and Engineering*, vol. 11, no. 2, p. 384, 2023.
- [9] M. A. R. Hashmi and R. H. Raza, “Novel demon spectra analysis techniques and empirical knowledge based reference criterion for acoustic signal classification,” *Journal of Electrical Engineering & Technology*, vol. 18, no. 1, pp. 561–578, 2023.
- [10] G. Hinton, O. Vinyals, and J. Dean, “Distilling the knowledge in a neural network,” in *NIPS Deep Learning and Representation Learning Workshop*, 2015. [Online]. Available: <http://arxiv.org/abs/1503.02531>
- [11] Z. Allen-Zhu and Y. Li, “Towards understanding ensemble, knowledge distillation and self-distillation in deep learning,” *arXiv preprint arXiv:2012.09816*, 2020.

- [12] A. Gordon, E. Eban, O. Nachum, B. Chen, H. Wu, T.-J. Yang, and E. Choi, "Morphnet: Fast & simple resource-constrained structure learning of deep networks," in *Proceedings of the IEEE conference on computer vision and pattern recognition*, 2018, pp. 1586–1595.
- [13] J. Wu, C. Leng, Y. Wang, Q. Hu, and J. Cheng, "Quantized convolutional neural networks for mobile devices," in *Proceedings of the IEEE conference on computer vision and pattern recognition*, 2016, pp. 4820–4828.
- [14] Y. Cheng, D. Wang, P. Zhou, and T. Zhang, "A survey of model compression and acceleration for deep neural networks," *arXiv preprint arXiv:1710.09282*, 2017.
- [15] C. Bucilua, R. Caruana, and A. Niculescu-Mizil, "Model compression," in *Proceedings of the 12th ACM SIGKDD international conference on Knowledge discovery and data mining*, 2006, pp. 535–541.
- [16] L. Beyer, X. Zhai, A. Royer, L. Markeeva, R. Anil, and A. Kolesnikov, "Knowledge distillation: A good teacher is patient and consistent," in *Proceedings of the IEEE/CVF conference on computer vision and pattern recognition*, 2022, pp. 10925–10934.
- [17] T. Huang, Y. Zhang, M. Zheng, S. You, F. Wang, C. Qian, and C. Xu, "Knowledge diffusion for distillation," *Advances in Neural Information Processing Systems*, vol. 36, 2024.
- [18] C. Shu, Y. Liu, J. Gao, Z. Yan, and C. Shen, "Channel-wise knowledge distillation for dense prediction," in *Proceedings of the IEEE/CVF International Conference on Computer Vision*, 2021, pp. 5311–5320.
- [19] S. Yang, A. Jin, X. Zeng, H. Wang, X. Hong, and M. Lei, "Underwater acoustic target recognition based on knowledge distillation under working conditions mismatching," *Multimedia Systems*, vol. 30, no. 1, p. 12, 2024.
- [20] B. Julesz, "Visual pattern discrimination," *IRE transactions on Information Theory*, vol. 8, no. 2, pp. 84–92, 1962.
- [21] G. Srinivasan and G. Shobha, "Statistical texture analysis," in *Proceedings of world academy of science, engineering and technology*, vol. 36, no. December, 2008, pp. 1264–1269.
- [22] J. S. Lim. *Two-dimensional signal and image processing*. Prentice-Hall, Inc., 1990.
- [23] M. Trevorrow, "Examination of statistics and modulation of underwater acoustic ship signatures," 2021.
- [24] G. Yu and J.-J. Slotine, "Fastwavelet-based visual classification," in *2008 19th International Conference on Pattern Recognition*. IEEE, 2008, pp. 1–5.
- [25] T. Serre, L. Wolf, S. Bileschi, M. Riesenhuber, and T. Poggio, "Robust object recognition with cortex-like mechanisms," *IEEE transactions on pattern analysis and machine intelligence*, vol. 29, no. 3, pp. 411–426, 2007.
- [26] X. Yin, X. Sun, P. Liu, L. Wang, and R. Tang, "Underwater acoustic target classification based on lofar spectrum and convolutional neural network," in *Proceedings of the 2nd International Conference on Artificial Intelligence and Advanced Manufacture*, 2020, pp. 59–63.
- [27] L. C. Domingos, P. E. Santos, P. S. Skelton, R. S. Brinkworth, and K. Sammut, "A survey of underwater acoustic data classification methods using deep learning for shoreline surveillance," *Sensors*, vol. 22, no. 6, p. 2181, 2022.
- [28] J. McDermott and E. Simoncelli, "Sound texture perception via statistics of the auditory periphery," 2011.
- [29] V.-S. Doan, T. Huynh-The, and D.-S. Kim, "Underwater acoustic target classification based on dense convolutional neural network," *IEEE Geoscience and Remote Sensing Letters*, vol. 19, pp. 1–5, 2020.
- [30] L. Chen, X. Luo, and H. Zhou, "A ship-radiated noise classification method based on domain knowledge embedding and attention mechanism," *Engineering Applications of Artificial Intelligence*, vol. 127, p. 107320, 2024.
- [31] H. I. Hummel, R. van der Mei, and S. Bhulai, "A survey on machine learning in ship radiated noise," *Ocean Engineering*, vol. 298, p. 117252, 2024.
- [32] H. Yang, K. Lee, Y. Choo, and K. Kim, "Underwater acoustic research trends with machine learning: Passive sonar applications," *Journal of Ocean Engineering and Technology*, vol. 34, no. 3, pp. 227–236, 2020.
- [33] E. L. Ferguson, R. Ramakrishnan, S. B. Williams, and C. T. Jin, "Convolutional neural networks for passive monitoring of a shallow water environment using a single sensor," in *2017 IEEE International Conference on Acoustics, Speech and Signal Processing (ICASSP)*. IEEE, 2017, pp. 2657–2661.
- [34] F. Yuan, X. Ke, and E. Cheng, "Joint representation and recognition for ship-radiated noise based on multimodal deep learning," *Journal of Marine Science and Engineering*, vol. 7, no. 11, p. 380, 2019.
- [35] C. Tan, F. Sun, T. Kong, W. Zhang, C. Yang, and C. Liu, "A survey on deep transfer learning," in *Artificial Neural Networks and Machine Learning—ICANN 2018: 27th International Conference on Artificial Neural Networks, Rhodes, Greece, October 4-7, 2018, Proceedings, Part III 27*. Springer, 2018, pp. 270–279.
- [36] K. Weiss, T. M. Khoshgoftaar, and D. Wang, "A survey of transfer learning," *Journal of Big data*, vol. 3, pp. 1–40, 2016.
- [37] A. Diment and T. Virtanen, "Transfer learning of weakly labelled audio," in *2017 IEEE workshop on applications of signal processing to audio and acoustics (waspa)*. IEEE, 2017, pp. 6–10.
- [38] J. Yim, D. Joo, J. Bae, and J. Kim, "A gift from knowledge distillation: Fast optimization, network minimization and transfer learning," in *Proceedings of the IEEE conference on computer vision and pattern recognition*, 2017, pp. 4133–4141.
- [39] A. M. Tripathi and K. Paul, "Data augmentation guided knowledge distillation for environmental sound classification," *Neurocomputing*, vol. 489, pp. 59–77, 2022.
- [40] F. Liu, H. Ding, D. Li, T. Wang, Z. Luo, and L. Chen, "Few-shot learning with data enhancement and transfer learning for underwater target recognition," in *2021 OES China Ocean Acoustics (COA)*. IEEE, 2021, pp. 992–994.
- [41] D. Cook, K. D. Feuz, and N. C. Krishnan, "Transfer learning for activity recognition: A survey," *Knowledge and information systems*, vol. 36, pp. 537–556, 2013.
- [42] K. Choi, M. Kersner, J. Morton, and B. Chang, "Temporal knowledge distillation for on-device audio classification," in *ICASSP 2022-2022 IEEE International Conference on Acoustics, Speech and Signal Processing (ICASSP)*. IEEE, 2022, pp. 486–490.
- [43] J.-W. Jung, H.-S. Heo, H.-J. Shim, and H.-J. Yu, "Knowledge distillation in acoustic scene classification," *IEEE Access*, vol. 8, pp. 166870–166879, 2020.
- [44] J. Ritu, E. Barnes, R. Martell, A. Van Dine, and J. Peeples, "Histogram layer time delay neural networks for passive sonar classification," in *2023 IEEE Workshop on Applications of Signal Processing to Audio and Acoustics (WASPAA)*. IEEE, 2023, pp. 1–5.
- [45] D. Ji, H. Wang, M. Tao, J. Huang, X.-S. Hua, and H. Lu, "Structural and statistical texture knowledge distillation for semantic segmentation," in *Proceedings of the IEEE/CVF Conference on Computer Vision and Pattern Recognition*, 2022, pp. 16876–16885.
- [46] L. Zhu, D. Ji, S. Zhu, W. Gan, W. Wu, and J. Yan, "Learning statistical texture for semantic segmentation," in *Proceedings of the IEEE/CVF Conference on Computer Vision and Pattern Recognition*, 2021, pp. 12537–12546.
- [47] Q. Tang, N. Sang, and T. Zhang, "Extraction of salient contours from cluttered scenes," *Pattern recognition*, vol. 40, no. 11, pp. 3100–3109, 2007.
- [48] P. J. Burt and E. H. Adelson, "The laplacian pyramid as a compact image code," in *Readings in computer vision*. Elsevier, 1987, pp. 671–679.
- [49] J. Peeples, S. A. Kharsa, L. Saleh, and A. Zare, "Histogram layers for neural engineered features," *arXiv preprint arXiv:2403.17176*, 2024.
- [50] Y. Zhang, T. Xiang, T. M. Hospedales, and H. Lu, "Deep mutual learning," in *Proceedings of the IEEE conference on computer vision and pattern recognition*, 2018, pp. 4320–4328.
- [51] M. Irfan, Z. Jiangbin, S. Ali, M. Iqbal, Z. Masood, and U. Hamid, "Deepship: An underwater acoustic benchmark dataset and a separable convolution based autoencoder for classification," *Expert Systems with Applications*, vol. 183, p. 115270, 2021.
- [52] Q. Kong, Y. Cao, T. Iqbal, Y. Wang, W. Wang, and M. D. Plumbley, "Panns: Large-scale pretrained audio neural networks for audio pattern recognition," *IEEE/ACM Transactions on Audio, Speech, and Language Processing*, vol. 28, pp. 2880–2894, 2020.
- [53] D. S. Park, W. Chan, Y. Zhang, C.-C. Chiu, B. Zoph, E. D. Cubuk, and Q. V. Le, "SpecAugment: A simple data augmentation method for automatic speech recognition," *arXiv preprint arXiv:1904.08779*, 2019.
- [54] Y. Wei and Y. Bai, "Dynamic temperature knowledge distillation," *arXiv preprint arXiv:2404.12711*, 2024.
- [55] J. Yang, X. Zhu, A. Bulat, B. Martinez, and G. Tzimiropoulos, "Knowledge distillation meets open-set semi-supervised learning," *International Journal of Computer Vision*, pp. 1–20, 2024.
- [56] L. Yuan, F. E. Tay, G. Li, T. Wang, and J. Feng, "Revisiting knowledge distillation via label smoothing regularization," in *Proceedings of the IEEE/CVF conference on computer vision and pattern recognition*, 2020, pp. 3903–3911.
- [57] Y. Tian, D. Krishnan, and P. Isola, "Contrastive representation distillation," in *International Conference on Learning Representations*.
- [58] Y. Zhang, Z. Lan, Y. Dai, F. Zeng, Y. Bai, J. Chang, and Y. Wei, "Prime-aware adaptive distillation," in *Computer Vision—ECCV 2020: 16th European Conference, Glasgow, UK, August 23–28, 2020, Proceedings, Part XIX 16*. Springer, 2020, pp. 658–674.



- [59] B. Peng, X. Jin, J. Liu, D. Li, Y. Wu, Y. Liu, S. Zhou, and Z. Zhang, "Correlation congruence for knowledge distillation," in *Proceedings of the IEEE/CVF International Conference on Computer Vision*, 2019, pp. 5007–5016.
- [60] Y. Matsubara, "torchdistill: A modular, configuration-driven framework for knowledge distillation," in *International Workshop on Reproducible Research in Pattern Recognition*. Springer, 2021, pp. 24–44.
- [61] L. Gao and H. Gao, "Feature decoupled knowledge distillation via spatial pyramid pooling," in *Proceedings of the Asian Conference on Computer Vision*, 2022, pp. 1109–1123.
- [62] C. Chen, J. Zhang, Y. Xu, L. Chen, J. Duan, Y. Chen, S. Tran, B. Zeng, and T. Chilimbi, "Why do we need large batchsizes in contrastive learning? a gradient-bias perspective," *Advances in Neural Information Processing Systems*, vol. 35, pp. 33 860–33 875, 2022.
- [63] P. Lu, A. Ghaddar, A. Rashid, M. Rezagholizadeh, A. Ghodsi, and P. Langlais, "Rw-kd: Sample-wise loss terms re-weighting for knowledge distillation," in *Findings of the Association for Computational Linguistics: EMNLP 2021*, 2021, pp. 3145–3152.
- [64] A. Psaltis, C. Chatzikonstantinou, C. Z. Patrikakis, and P. Daras, "Fedrcil: Federated knowledge distillation for representation based contrastive incremental learning," in *Proceedings of the IEEE/CVF International Conference on Computer Vision*, 2023, pp. 3463–3472.